Journal of Computational Physics 374 (2018) 478–494

Contents lists available at ScienceDirect

Journal of Computational Physics

www.elsevier.com/locate/jcp

# Versatile and accurate schemes of discretization for the electromagnetic scattering analysis of arbitrarily shaped piecewise homogeneous objects

Ivan Sekulic*, Eduard Ubeda, Juan M. Rius

*CommSensLab, Universitat Politecnica de Catalunya (BarcelonaTech), Jordi Girona 1-3, 08034 Barcelona, Spain*

ARTICLE INFO

*Article history:*
Received 21 March 2018
Received in revised form 12 July 2018
Accepted 18 July 2018
Available online 20 July 2018

*Keywords:*
Composite objects
Integral equations
Method of moments (MoM)
Electric-field integral equation (EFIE)
Poggio–Miller–Chang–Harrington–Wu–Tsai (PMCHWT) formulation
Nonconformal meshes

ABSTRACT

The discretization by the method of moments (MoM) of integral equations in the electromagnetic scattering analysis most often relies on divergence-conforming basis functions, such as the Rao–Wilton–Glisson (RWG) set, which preserve the normal continuity of the expanded currents across the edges arising from the discretization of the target boundary. Although for such schemes the boundary integrals become free from hypersingular kernel-contributions, which is numerically advantageous, their practical implementation in real-life scenarios becomes particularly cumbersome. Indeed, the application of the normal continuity condition on composite objects becomes elaborate and convoluted at junction-edges, where several regions intersect. Also, such edge-based schemes cannot even be applied to nonconformal meshes, where adjacent facets may not share single matching edges. In this paper, we present nonconforming schemes of discretization for the scattering analysis of complex objects based on the expansion of the boundary unknowns, electric or magnetic currents, with the facet-based monopolar-RWG set. We show with examples how these schemes exhibit great flexibility when handling composite piecewise homogeneous objects with junctions or targets modeled with nonconformal meshes. Furthermore, these schemes offer improved near- and far-field accuracy in the scattering analysis of electrically small single sharp-edged dielectric targets with moderate or high dielectric contrasts.



## 1. Introduction

The accurate scattering analysis of complex targets, made up of homogeneous components with different electromagnetic properties, is of great interest nowadays for the engineering community. The surface integral equations, such as the electric-field integral equation (EFIE) [1] and the Poggio–Miller–Chang–Harrington–Wu–Tsai (PMCHWT) [2–4] formulation, arise from setting currents and field boundary conditions over the surface interfaces between different regions. These schemes, which satisfy by definition the radiation condition at infinity, are normally preferred in the scattering analysis of homogeneous targets, perfectly conducting (PEC) or penetrable, over other numerical schemes, such as the volume integral equations [5], which require the definition of unknowns inside regions, or the finite-element methods [6,7] which call for the explicit insertion of absorbing boundary conditions [8]. In the Galerkin discretization by the method of moments

* Corresponding author.
*E-mail addresses:* ivan.sekulic@tsc.upc.edu (I. Sekulic), ubeda@tsc.upc.edu (E. Ubeda), rius@tsc.upc.edu (J.M. Rius).

https://doi.org/10.1016/j.jcp.2018.07.034
0021-9991/

[9] of surface-integral equations, the currents and the tangential traces of the field spaces over the boundary interfaces are expanded and tested, respectively, with the same set of basis functions. Typically, these are divergence-conforming sets, such as the RWG set, which enforce normal continuity across the edges arising from the discretization and span a finite-dimensional subspace inside $\mathcal{H}^{-1/2}(\mathrm{div}_{\partial\Omega}, \partial\Omega)$ [10], the function space that encompasses the space of currents and the dual of the range of the tangential-trace operators [11–13]. Galerkin-discretizations with the RWG basis functions of the EFIE and PMCHWT formulations [1,14] excel as conforming schemes, hence with converging solutions in the physical space of currents [15,16]. Moreover, these implementations are numerically advantageous because the hypersingular kernel contributions cancel out.

The well-established conforming scattering analysis for single homogeneous objects can be extended straightforwardly to composite objects without junctions, such as coated metallic objects or multilayered penetrable structures [17,18]. However, the development of conforming schemes for composite objects with junctions, viz. boundary lines where more than two regions intersect, becomes somewhat awkward because of the definition of special continuity conditions at junctions [19–23]. In any case, these *single-surface* (or *single-trace*) approaches have been successful for decades in the analysis of composite structures despite the involved search of junctions and the required identification of the number and type (metallic or penetrable) of intersecting regions at each junction. More recently, other so-called *two-surface* [24] or *multi-trace* [25] schemes circumvent the management of junctions by treating the composite object as a set of disjoint objects immersed in a host medium, with the separation distances tending to zero. These schemes provide improved flexibility when managing composite objects but require the definition of additional redundant unknowns at touching surfaces. Clearly, the single-trace approaches were developed in earlier times, with restricted computational resources, such that the definition of additional unknowns was just too costly. Conversely, over the past years, the double-surface and multi-trace schemes have captured the attention of researchers thanks to the dramatic increase of available memory resources.

All these schemes suffer from the mesh restrictions imposed by the adopted divergence-conforming sets, which need to be defined over conformal meshes, with all pairs of adjacent facets sharing a single edge. In consequence, the mesh generation of composite objects in the single-trace analysis becomes especially constrained, inadequate to combine arbitrary meshes arising from the independent tessellation of each of the several subdomains that form the original structure. Similarly, although the double-surface and multi-trace techniques allow the juxtaposition of closed meshes linked to each subdomain, the meshing schemes adopted must be in any case locally conformal over each subdomain. Hence, the application of such schemes to nonconformal meshes, where adjacent facets may not share single edges, appears unworkable. This has some impact in the analysis of real-life complex structures, especially when the mesh under analysis arises from the interconnection of open arbitrary triangulations.

In this work, we address the robust, accurate and versatile single-surface scattering analysis of dielectric objects with arbitrary shape and composite objects with junctions. For this, we employ the EFIE–PMCHWT integral-equation formulation [21], which follows from the application of the EFIE or PMCHWT formulations over boundary surfaces, respectively, enclosing PEC regions or separating penetrable regions. The proposed schemes rely on the expansion of the currents with the facet-based, discontinuous-across-edges, monopolar-RWG set [26–29]. This choice gives rise to boundary integrals with hypersingular kernels, which we handle by testing the equations with well-suited testing functions defined off the boundary tessellation, inside the region where, in light of the surface equivalence principle, the fields must be zero. The *volumetric* scheme of testing defines the testing functions over small volumetric domains, tetrahedral elements or wedges, attached to the boundary surface [27,28]. The *tangential-normal* scheme deploys RWG testing functions over pairs of adjacent triangles such that one triangle matches a boundary triangle and the other one is quasi-normally oriented into the null-field region [29]. These implementations are nonconforming since the finite-dimensional spaces spanned by the monopolar-RWG functions belong to the space of square-integrable functions $L^2(\partial\Omega)$ [30]. Interestingly, they exhibit similar or better accuracy than the conventional RWG-schemes in the scattering analysis of targets with sharp edges and corners, PEC [27–29,31] or 2D TE-dielectric [32], especially if moderately small. Note that for a given discretization the monopolar-RWG space includes the space spanned by the RWG basis functions [27].

As we show in the paper, our nonconforming PMCHWT implementations exhibit improved accuracy when compared with the RWG-schemes in the analysis of single small sharp-edged dielectric objects with moderate or high dielectric contrasts. Moreover, our schemes manifest in general great flexibility in the single-surface analysis of composite objects with junctions as the special modeling of currents at junctions is not required. Also, the proposed implementations can handle nonconformal meshes when applied to piecewise (or fully) homogeneous arbitrarily shaped objects. This represents significant progress with respect to previous schemes, mainly addressing nonconformal meshes of homogeneous 3D targets, PEC [27–30] or dielectric [33,34], or 2D composite objects [32]. Our schemes become also well suited for the enhancement of integral-equation domain decomposition methods [34–36], since the transmission conditions between contiguous subdomains may be satisfied through the off-boundary testing and the discontinuous monopolar-RWG expansion.

In Section 2, details on the monopolar-RWG discretization of the PMCHWT formulation, with off-boundary testing, are provided. Special emphasis is given on the wedge volumetric and the tangential-normal schemes of testing, while details on the tetrahedral testing are already available in [37]. In Section 3, the analysis of piecewise homogeneous composite objects with the monopolar-RWG discretization of the single-surface EFIE–PMCHWT formulation is described. The difficulties in the management of junctions with the conventional schemes are described together with the advantages of our nonconforming discretizations. In Section 4, results for the various monopolar-RWG schemes of discretization of the EFIE–PMCHWT formulation, with volumetric or tangential-normal testing, are shown and discussed.

## 2. Nonconforming PMCHWT for single penetrable targets

The scattering analysis of an arbitrarily shaped penetrable body immersed in a host medium is usually carried out through the equivalent definition of the original problem in terms of two homogeneous problems associated with each of the two regions, outside ($i = 1$) or inside ($i = 2$) the body (see Fig. 1). The scattered fields $\boldsymbol{E}_i^s$ and $\boldsymbol{H}_i^s$ are generated in the homogeneous problem associated with the region $i$ by $\boldsymbol{J}_i$ and $\boldsymbol{M}_i$, respectively, the electric and magnetic currents defined at the side of the boundary surface $\partial\Omega$ inside the region $i$. In light of the equivalence theorem, the total fields, resulting from the summation of the incident and scattered fields, are zero in the equivalent problem out of the corresponding regions (see Fig. 1). In this paper, we expand the unknown currents $\boldsymbol{J}_i$ and $\boldsymbol{M}_i$ with the monopolar-RWG set of basis functions $\{\boldsymbol{f}_n^p\} \in \boldsymbol{L}^2(\partial\Omega)$ as follows [26]

$$\boldsymbol{J}_i \simeq \sum_{n=1}^{N_t} J_n^{p,i} \boldsymbol{f}_n^p \tag{1}$$

$$\boldsymbol{M}_i \simeq \sum_{n=1}^{N_t} M_n^{p,i} \boldsymbol{f}_n^p \quad i = 1, 2 \quad p = 1, 2, 3 \tag{2}$$

where $\{J_n^{p,i}\}$ and $\{M_n^{p,i}\}$ represent the sets of unknown coefficients in the expansion of the currents and $N_t$ denotes the number of triangles arising from the discretization of the boundary surface.

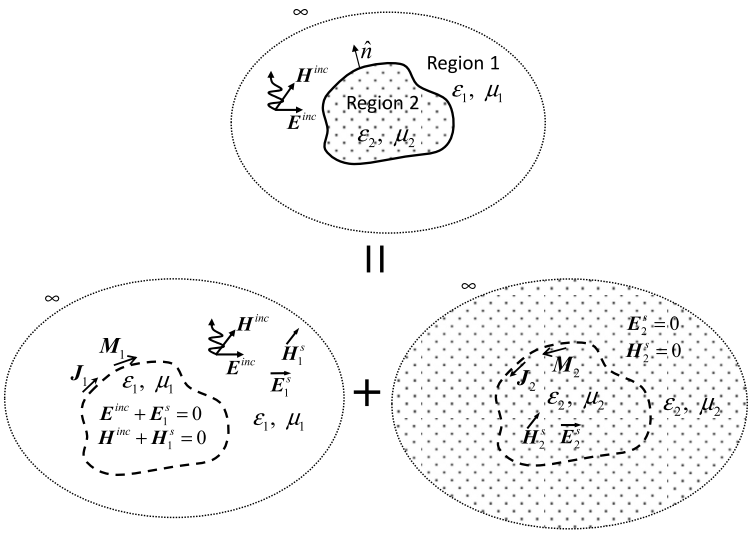


**Fig. 1.** Surface equivalence theorem for a penetrable object and plane wave excitation.

The monopolar-RWG and RWG basis functions share the same definition inside each triangle [26–29]. However, whereas the RWG set is edge-based, with a normally continuous transition across edges, the monopolar-RWG set is facet-based, with no continuity imposition across edges. In consequence, for a given closed triangulation, the RWG discretization handles as many unknowns as the number of edges, while the monopolar-RWG set gives rise to twice this amount of unknowns or, equivalently, three times the number of triangles. The subsets $\{\boldsymbol{f}_n^1\}$, $\{\boldsymbol{f}_n^2\}$ and $\{\boldsymbol{f}_n^3\}$ denote the three monopolar-RWG contributions sharing the $n$th triangle $S_n$ so that

$$\boldsymbol{f}_n^p(\mathbf{r}') = \frac{1}{2A_n}(\mathbf{r}' - \mathbf{r}_n^p) \quad \mathbf{r}' \in S_n \tag{3}$$

where $\mathbf{r}_n^1$, $\mathbf{r}_n^2$, $\mathbf{r}_n^3$ represent the position vectors of the three vertices of $S_n$, with area $A_n$ (see Fig. 2).

The approximated scattered fields generated in the homogeneous problem associated with the region $i$ are defined as [37]

$$\tilde{\boldsymbol{E}}_i^s \simeq \sum_{n=1}^{N_t} \eta_i \boldsymbol{T}_n^{p,i} J_n^{p,i} - \sum_{n=1}^{N_t} \boldsymbol{K}_n^{p,i} M_n^{p,i} \tag{4}$$

$$\tilde{\boldsymbol{H}}_i^s \simeq \sum_{n=1}^{N_t} \boldsymbol{K}_n^{p,i} J_n^{p,i} + \sum_{n=1}^{N_t} \frac{1}{\eta_i} \boldsymbol{T}_n^{p,i} M_n^{p,i} \tag{5}$$

with

$$\boldsymbol{K}_n^{p,i}(\boldsymbol{r}) = \nabla \times \iint_{S_n} G_i(\boldsymbol{r}, \boldsymbol{r}') \boldsymbol{f}_n^p(\boldsymbol{r}') dS' \tag{6}$$

$$\boldsymbol{T}_n^{p,i}(\boldsymbol{r}) = -jk_i \iint_{S_n} G_i(\boldsymbol{r}, \boldsymbol{r}') \boldsymbol{f}_n^p(\boldsymbol{r}') dS' - j\frac{1}{k_i} \nabla \Phi_n^{p,i}(\boldsymbol{r}) \tag{7}$$

The scalar function $\Phi_n^{p,i}(\boldsymbol{r})$, from which the discretized electric and magnetic scalar potentials are derived, is defined in general as [38]

$$\Phi_n^{p,i}(\boldsymbol{r}) = \iint_{S_n} G_i(\boldsymbol{r}, \boldsymbol{r}') \nabla' \cdot \boldsymbol{f}_n^p(\boldsymbol{r}') dS' - \oint_{\partial S_n} G_i(\boldsymbol{r}, \boldsymbol{r}') \boldsymbol{f}_n^p(\boldsymbol{r}') \cdot \hat{n}_c^n dl' \tag{8}$$

where $\partial S_n$ and $\hat{n}_c^n$ denote, respectively, the closed contour around the source triangle and the unit vector perpendicular to this contour. The function $G_i$ represents the Green's function of the homogeneous problem associated with the region $i$; that is,

$$G_i(\boldsymbol{r}, \boldsymbol{r}') = \frac{e^{-jk_i R}}{4\pi R}, \quad R = |\boldsymbol{r} - \boldsymbol{r}'| \tag{9}$$

The constants $k_i$ and $\eta_i$ stand for the wave number and the impedance of the region $i$, respectively, and are expressed in terms of the free-space constants, $k_0$ and $\eta_0$, as

$$k_i = k_0 \sqrt{\varepsilon_{r,i} \cdot \mu_{r,i}}, \qquad \eta_i = \eta_0 \sqrt{\frac{\mu_{r,i}}{\varepsilon_{r,i}}} \tag{10}$$

where $\varepsilon_{r,i}$ and $\mu_{r,i}$ denote, respectively, the relative permittivity and the relative permeability in the $i$-th region.

The discretized PMCHWT formulation imposes the electric-field and magnetic-field boundary conditions over the two sides ($i = 1, 2$) of the meshed boundary surface $\tilde{S} = \bigcup_{n=1}^{N_t} S_n$ so that

$$\left(\tilde{\boldsymbol{E}}_1^s - \tilde{\boldsymbol{E}}_2^s\right)_{\tilde{S},\tan} \simeq \sum_{n=1}^{N_t} \left(\eta_1 \boldsymbol{T}_n^{p,1} + \eta_2 \boldsymbol{T}_n^{p,2}\right)_{\tilde{S},\tan} J_n^p - \sum_{n=1}^{N_t} \left(\boldsymbol{K}_n^{p,1} + \boldsymbol{K}_n^{p,2}\right)_{\tilde{S},\tan} M_n^p \simeq -\boldsymbol{E}_{\tilde{S},\tan}^{inc} \tag{11}$$

$$\left(\tilde{\boldsymbol{H}}_1^s - \tilde{\boldsymbol{H}}_2^s\right)_{\tilde{S},\tan} \simeq \sum_{n=1}^{N_t} \left(\boldsymbol{K}_n^{p,1} + \boldsymbol{K}_n^{p,2}\right)_{\tilde{S},\tan} J_n^p + \sum_{n=1}^{N_t} \left(\frac{1}{\eta_1} \boldsymbol{T}_n^{p,1} + \frac{1}{\eta_2} \boldsymbol{T}_n^{p,2}\right)_{\tilde{S},\tan} M_n^p \simeq -\boldsymbol{H}_{\tilde{S},\tan}^{inc} \tag{12}$$

where $\boldsymbol{E}^{inc}$ and $\boldsymbol{H}^{inc}$ stand for the incident electric and magnetic fields, respectively, and $\boldsymbol{K}_n^{p,1}$, $\boldsymbol{K}_n^{p,2}$ are considered in the Cauchy principal value sense. The currents at both sides of the boundary surface are related such that the tangential boundary condition is satisfied; i.e. $J_n^p = J_n^{p,1} = -J_n^{p,2}$ and $M_n^p = M_n^{p,1} = -M_n^{p,2}$.

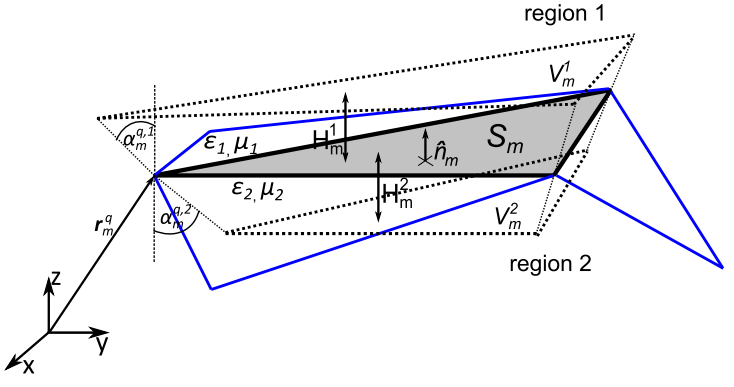


**Fig. 2.** $m$th triangle arising from the discretization of the boundary surface where the volumetric wedge testing scheme is defined conformal to the surface.

We cast the equations (11) and (12) into matrix form by testing the tangential field conditions with an appropriate set of testing functions. The commonly used Galerkin formulation, which adopts the same set for testing the fields and expanding the currents, gives rise to

$$\iint_{S_m} \left(\tilde{\boldsymbol{E}}_1^s - \tilde{\boldsymbol{E}}_2^s\right) \cdot \boldsymbol{f}_m^q(\boldsymbol{r}) dS = -\iint_{S_m} \boldsymbol{E}^{inc} \cdot \boldsymbol{f}_m^q(\boldsymbol{r}) dS$$
$$\iint_{S_m} \left(\tilde{\boldsymbol{H}}_1^s - \tilde{\boldsymbol{H}}_2^s\right) \cdot \boldsymbol{f}_m^q(\boldsymbol{r}) dS = -\iint_{S_m} \boldsymbol{H}^{inc} \cdot \boldsymbol{f}_m^q(\boldsymbol{r}) dS \quad m = 1 \ldots N_t \quad q = 1, 2, 3 \tag{13}$$

The Galerkin testing of the electric or magnetic field traces in (13) gives rise to hypersingular kernel contributions, linked to the double gradient of the Green's function, that can be directly evaluated through elaborate analytical formulas [39]. Alternatively, the integration by parts of these double gradient kernel contributions leads to contour-surface or double-surface integrals, easy-to-manage through well-known integration routines, and to double-contour integrals, which become unbounded for self- or edge-adjacent interactions. Over the last years, several strategies have been proposed to make the latter contributions numerically manageable; namely, compensating the double-contour integrals through the introduction of the so-called *penalty terms* [26]; singling out the critical term that makes the near interactions infinitely large [40]; or testing the fields over small volumetric or surface domains attached to the boundary surface, inside the region where the fields must be zero [27–29]. In this paper, we adopt the latter choice, for which several non-Galerkin testing procedures can be defined (volumetric or tangential-normal).

### 2.1. Volumetric testing

We test the scattered fields through a set of testing functions $\{\boldsymbol{w}_m^{q,i}\}$ defined over a set of wedge elements, $\{V_m^i\}$, attached to the boundary-surface inside the region $i$, where the null-field condition must be accomplished according to the equivalence principle (Fig. 2). This scheme is analogous to the volumetric nonconforming EFIE implementation for conductors [28], where the volumetric domains are located inside the object. The wedges can be defined either *conformal* or *nonconformal* to the boundary. In the former, the wedges are bounded by three trapezoids that lie in the planes bisecting the angles formed by the corresponding triangle arising in the surface tessellation and the three neighboring triangles (Fig. 2). In the latter, the testing elements are defined as right triangular prisms. This choice appears as particularly flexible and versatile because no a priori knowledge of the boundary shape is required and because nonconformal meshes can be handled. However, for triangles with an edge touching a sharp corner, the testing wedge will break out of the null-field region and some numerical error may appear.

We define the volumetric wedge testing functions [28] as:

$$\boldsymbol{w}_m^{q,i}(\boldsymbol{r}) = \frac{1}{2A_m H_m^i}\left[\boldsymbol{\rho}_m^q - \left(\boldsymbol{r}_m^q - \boldsymbol{r}\right) \cdot \hat{n}_m \tan\alpha_m^{q,i} \cdot \hat{\rho}_m^q\right] \quad \boldsymbol{r} \in V_m^i \quad i = 1, 2 \quad q = 1, 2, 3 \quad m = 1 \ldots N_t \tag{14}$$

where $\boldsymbol{\rho}_m^q$ represents the projection of the vector $(\boldsymbol{r} - \boldsymbol{r}_m^q)$ onto the plane of the triangle $S_m$ and $H_m^i$ denotes the height of the wedge associated with the field triangle $S_m$. This parameter is defined as a fraction of the mesh parameter, which we set as the average length of the side segments of $S_m$ and has the same value at both regions ($i = 1, 2$). The unit vector $\hat{n}_m$ is oriented normally with respect to $S_m$ and points from region 2 to region 1; $\alpha_m^{q,i}$ denotes the angle of the side edge of the $m$-th wedge associated with the $q$-th vertex with respect to $\hat{n}_m$ (see Fig. 2). For testing elements nonconformal to the boundary $\alpha_m^{q,i} = 0$, whereby the second term on the right hand side of (14) disappears.

The volumetrically tested monopolar-RWG discretization of the PMCHWT leads to the following matrix system [32]

$$\iiint_{V_m^2} \tilde{\boldsymbol{E}}_1^s \cdot \boldsymbol{w}_m^{q,2}(\boldsymbol{r}) dV - \iiint_{V_m^1} \tilde{\boldsymbol{E}}_2^s \cdot \boldsymbol{w}_m^{q,1}(\boldsymbol{r}) dV = -\iiint_{V_m^2} \boldsymbol{E}^{inc} \cdot \boldsymbol{w}_m^{q,2}(\boldsymbol{r}) dV \tag{15}$$

$$\iiint_{V_m^2} \tilde{\boldsymbol{H}}_1^s \cdot \boldsymbol{w}_m^{q,2}(\boldsymbol{r}) dV - \iiint_{V_m^1} \tilde{\boldsymbol{H}}_2^s \cdot \boldsymbol{w}_m^{q,1}(\boldsymbol{r}) dV = -\iiint_{V_m^2} \boldsymbol{H}^{inc} \cdot \boldsymbol{w}_m^{q,2}(\boldsymbol{r}) dV \tag{16}$$

Indeed, the double contour integrals in (13) now disappear since the surface testing integrals of the Galerkin testing are replaced by volumetric integrals. The accuracy of this implementation can be fine-tuned by adjusting the height of the wedge elements. In practice, the recently introduced testing with tetrahedral elements [37], which stands for an alternative scheme of volumetric testing, becomes easier to implement than the wedge testing. On the other hand, the tetrahedral testing provides improved accuracy in the scattering analysis of single dielectric objects for a smaller range of heights than the wedge testing, especially in far-field computation (see Figs. 6 and 7).

### 2.2. Tangential-normal testing

The fields are tested over a pair of edge-adjacent triangles such that one triangle matches a facet arising in the surface triangulation, and the other one is oriented quasi-normally inside the region where the field becomes zero according to the equivalence theorem (see Fig. 3). This scheme is analogous to the nonconforming EFIE implementation introduced in [29] for conductors and can also be defined *conformal* or *nonconformal* to the boundary depending on whether the off-boundary triangle lies in the plane bisecting the angle between two edge-adjacent triangles or is oriented normally with respect to the matching triangle (see Fig. 3). The testing integrals are now surface integrals, which alleviates the computational effort otherwise required for the volumetric integrals in (15) and (16).

We define the tangential-normal testing functions $\{\boldsymbol{t}_m^{q,i}\}$ as RWG basis functions so that

$$\boldsymbol{t}_m^{q,i}(\boldsymbol{r}) = \begin{cases} \boldsymbol{f}_m^q(\boldsymbol{r}) & \boldsymbol{r} \in S_m \\ -\boldsymbol{g}_m^{q,i}(\boldsymbol{r}) & \boldsymbol{r} \in S_m^{q,i} \end{cases} \quad i = 1,2 \quad q = 1,2,3 \quad m = 1 \ldots N_t \tag{17}$$

where $\boldsymbol{f}_m^q(\boldsymbol{r})$ and $\boldsymbol{g}_m^{q,i}(\boldsymbol{r})$ denote the two RWG contributions, respectively, over the surface triangle $S_m$ and over the triangle $S_m^{q,i}$, oriented quasi-normally inside the region $i$ (see Fig. 3) and defined as

$$\boldsymbol{g}_m^{q,i}(\boldsymbol{r}) = \frac{1}{2A_m^{q,i}}\left(\boldsymbol{r} - \boldsymbol{r}_m^{q,i}\right) \tag{18}$$

where $\boldsymbol{r}_m^{q,i}$ and $A_m^{q,i}$ represent, respectively, the position vector of the off-boundary vertex and the area of $S_m^{q,i}$ (see Fig. 3).

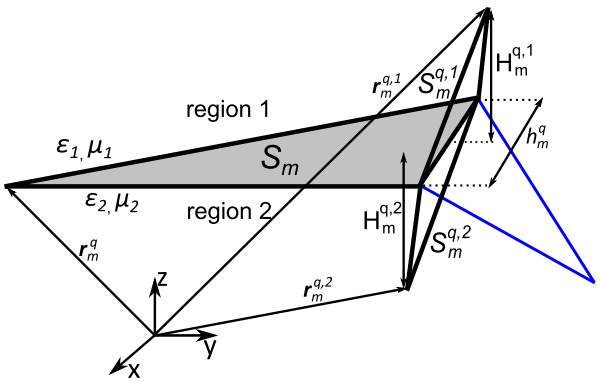


**Fig. 3.** $m$th triangle arising from the discretization of the boundary surface where the tangential-normal testing scheme is defined conformal to the surface.

The monopolar-RWG discretization of the PMCHWT formulation with tangential-normal testing gives rise to the following matrix system [32]

$$\iint\limits_{S_m \cup S_m^{q,2}} \tilde{\boldsymbol{E}}_1^s \cdot \boldsymbol{t}_m^{q,2}(\boldsymbol{r}) dS - \iint\limits_{S_m \cup S_m^{q,1}} \tilde{\boldsymbol{E}}_2^s \cdot \boldsymbol{t}_m^{q,1}(\boldsymbol{r}) dS = - \iint\limits_{S_m \cup S_m^{q,2}} \boldsymbol{E}^{inc} \cdot \boldsymbol{t}_m^{q,2}(\boldsymbol{r}) dS \tag{19}$$

$$\iint\limits_{S_m \cup S_m^{q,2}} \tilde{\boldsymbol{H}}_1^s \cdot \boldsymbol{t}_m^{q,2}(\boldsymbol{r}) dS - \iint\limits_{S_m \cup S_m^{q,1}} \tilde{\boldsymbol{H}}_2^s \cdot \boldsymbol{t}_m^{q,1}(\boldsymbol{r}) dS = - \iint\limits_{S_m \cup S_m^{q,2}} \boldsymbol{H}^{inc} \cdot \boldsymbol{t}_m^{q,2}(\boldsymbol{r}) dS \tag{20}$$

where the testing of the gradients of the scalar potentials can be simplified through

$$\iint\limits_{S_m \cup S_m^{q,i}} \boldsymbol{t}_m^{q,i} \cdot \nabla \Phi_n^{p,i} dS = - \iint\limits_{S_m \cup S_m^{q,i}} \Phi_n^{p,i} \nabla \cdot \boldsymbol{t}_m^{q,i} dS \tag{21}$$

because $\iint_{S_m \cup S_m^{q,i}} \nabla \cdot (\boldsymbol{t}_m^{q,i} \Phi_n^{p,i}) dS = 0$ thanks to the normal continuity of $\boldsymbol{t}_m^{q,i}$ across the common edge between the triangles $S_m$ and $S_m^{q,i}$. The accuracy of this implementation is fine-tuned by adjusting the height $H_m^{q,i}$ of the testing triangle $S_m^{q,i}$, which we define with the same value in both regions as a fraction of $h_m^q$, the length of the $q$th side in $S_m$, which is shared with $S_m^{q,i}$ (see Fig. 3).

## 3. Nonconforming EFIE–PMCHWT for piecewise homogeneous objects with junctions

The single-surface RWG-discretization of the EFIE–PMCHWT formulation for a composite object out of junction-edges, as shown in [21], is defined in an analogous manner as the Galerkin RWG-discretization of the EFIE [1] or the PMCHWT formulation [14] for a single object. At junction-edges, though, specially tailored schemes need to be defined in order to enforce the continuity conditions [19–23]. These techniques have become widespread over the last decades because of the observed good accuracy and the restrained number of unknowns. The use of moderate number of unknowns was particularly compelling in earlier times, when the computational resources were limited. However, the establishment of the continuity conditions at junctions demands some previous insight into the mesh topology in order to identify edges and junctions, which may actually be rather time-consuming for intricate or fine meshes, and gives rise in general to additional bookkeeping effort in the matrix generation.

In Fig. 4 we show the section of a rather simple composite object with junctions. Whereas in junction [C] all the intersecting regions are penetrable, in junctions [A], [B] and [D] one of the regions is perfectly conducting. Whereas the electric-field and electric-current continuity conditions need to be enforced around all these junctions, junction [C] requires also the imposition of the normal continuity in the expansion/testing, respectively, of the magnetic current/field. In consequence, unlike the single penetrable objects, where the boundary unknowns are invoked only by the two homogeneous problems of the equivalence theorem, the unknowns associated with junction [C] need to be simultaneously invoked by the homogeneous problems associated with the regions 1, 2 and 3. Similarly, the unknowns associated with junctions [A], [B] and [D], which share a PEC-region, are invoked by the homogeneous problems associated with different pairs of regions, respectively, 1–2, 2–3 and 1–3. It is hence clear that the single-surface RWG analysis of a composite object with an arbitrary number of junctions and a different number and type of intersecting regions each will require significant effort.

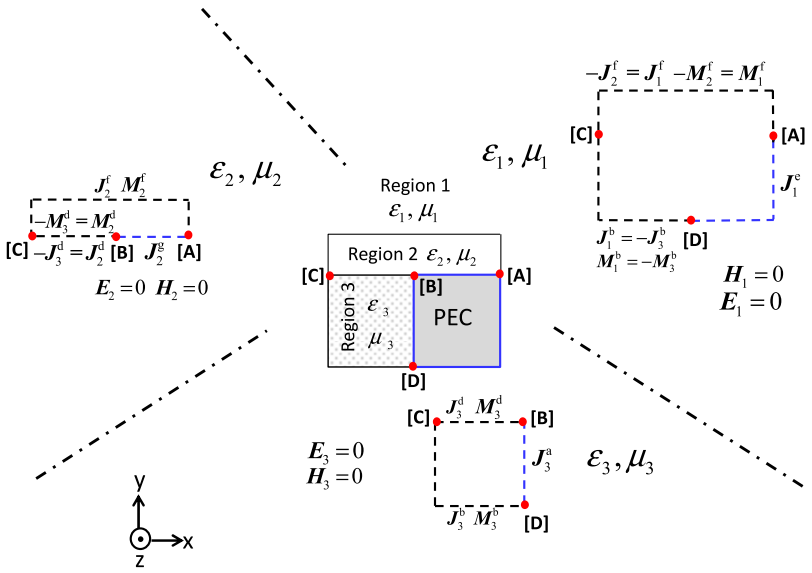


**Fig. 4.** Surface equivalence theorem applied to a composite object with two penetrable regions and one PEC region. *xy*-plane cross section of the composite object is presented. The dashed lines denote surface interfaces between regions. The nodes denote junctions.

The single-surface RWG-discretization of the EFIE–PMCHWT formulation can handle meshes, such as Fig. 5(a), where the intersecting regions at junctions are conformal at the junction as long as the appropriate treatment at junctions is applied [19–23]. However, this approach cannot address the analysis of nonconformal meshes meeting at junctions, arising very often from the juxtaposition of independently meshed targets, such as for example Fig. 5(c). Alternative conforming implementations of the EFIE–PMCHWT formulation, double-surface or multi-trace, are obtained by representing the composite object as a union of disjoint homogeneous regions immersed in the host medium with separation distances ($\delta$) tending to zero (see Fig. 5(b) and Fig. 5(d)). The original interfaces between two regions are now considered as two contact surfaces and thus junction-edges, which result from the intersection of more than two regions, do not exist. The programming burden of these approaches is alleviated when compared with the single-surface approach because the treatment of junction-edges is avoided. However, the number of unknowns rises because of the definition of redundant unknowns over touching interfaces. Although nowadays, in a context of sufficient memory resources, this requirement may seem of minor importance, in earlier times could become prohibitive. Moreover, the two-surface analysis [24] requires the computation of the residues of the integrals in (6), in addition to the Cauchy principal values, so that the tangential field continuity conditions are satisfied between touching regions. This becomes especially tricky if the touching meshes are nonmatching, as in Fig. 5(d).

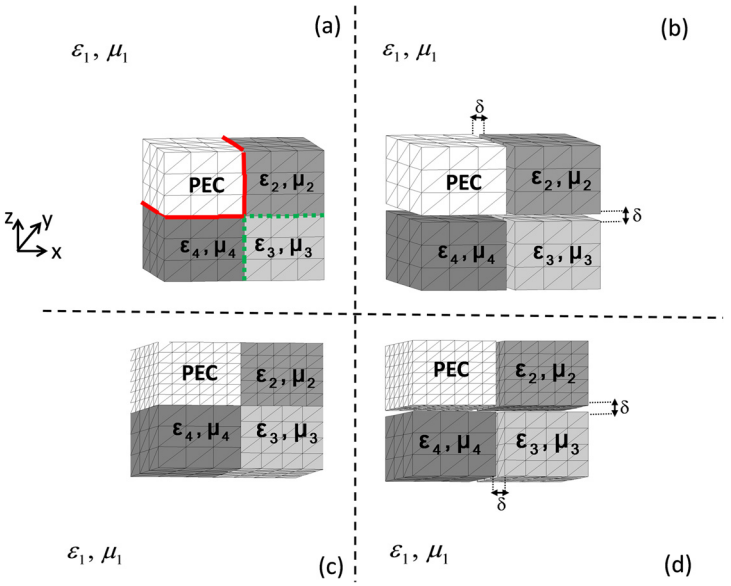


**Fig. 5.** Analysis of composite objects. (a) Single-surface interfaces and conformal segmentations. (b) Two-surface interfaces and conformal segmentations ($\delta \to 0$). (c) Single-surface interfaces and nonconformal segmentations. (d) Two-surface interfaces and nonconformal segmentations ($\delta \to 0$).

In this paper, we present a single-surface implementation of the EFIE–PMCHWT formulation that allows the agile scattering analysis of arbitrary composite objects with junctions. We expand the currents with the monopolar-RWG basis functions and we test the field-boundary conditions over off-boundary domains. Importantly, whereas the electric currents (or fields) are expanded (or tested) over all sorts of interface surfaces, the analogous magnetic magnitudes need to be defined only at interfaces between penetrable regions. Since the monopolar-RWG basis functions and the off-boundary testing schemes are facet-based, these approaches by construction ignore junctions. This is very advantageous because, unlike junction-edges, which arise from the intersection of several regions, all the facets arising from the discretization of an arbitrary composite object separate two regions only. Therefore, these schemes invoke the same number of homogeneous problems in the analysis of composite objects as in the analysis of single objects. Namely, two if the bordering regions are penetrable and one if one region is PEC. In general, our approach exhibits great flexibility when handling composite objects discretized with conformal meshes, as in Fig. 5(a), because the special treatment of junctions of the conventional schemes is avoided. Moreover, the single-surface nonconforming analysis of the nonconformal mesh in Fig. 5(c), where the single-surface RWG-implementation fails because the two overlapping meshes do not match, is carried out through the expansion (or testing) of the electric or magnetic currents (or fields) over a different overlapping triangulation each.

The generation of the impedance matrix elements in our nonconforming schemes becomes more elaborate than with the conventional RWG-schemes because line or volumetric integrals are computed. However, in our experience, this computational load is counterbalanced with the easier management of facet-to-facet interactions and the one or two invoked homogeneous problems for each interaction. Furthermore, it is well understood that these facet-based schemes do not demand search for edges or junctions as is required for the edge-based schemes. Note that the edge-search procedures become difficult and time-consuming for intricate and dense meshes and are bound to be fruitless for nonconformal or defective meshes.

## 4. Numerical results

In section 4.1, we focus on the scattering analysis with our single-surface monopolar-RWG PMCHWT-implementations of several single penetrable objects discretized with conformal meshes. In subsections A and B, we show the observed improved accuracy versus, respectively, the heights of the testing elements ($H$) and the number of unknowns ($N$). Several schemes of testing are used: wedge volumetric, PMCHWT[vol-wed], tetrahedral volumetric, PMCHWT[vol-tet], or tangential-normal, PMCHWT[tn]. The accuracies are checked against the conventional RWG discretization of the PMCHWT, PMCHWT[R], which can be used because the adopted meshes are conformal. The tested objects have sharp edges and corners and moderate or high dielectric contrasts because it is in these cases where the observed improved accuracy is especially evident. In the scattering analysis of dielectric targets with smooth boundaries and/or low relative permittivities, where singular field behavior does not occur [41], our schemes offer for a given meshing similar accuracy as the conventional RWG approaches but doubling the number of unknowns. Analogous observations have been reported in the scattering analysis of conductors [27] or 2D dielectrics [32] with the nonconforming discretization of, respectively, the EFIE and the TE-PMCHWT formulations.

In section 4.2 we show the suitability of our monopolar-RWG implementations in the analysis of various single or composite objects discretized with nonconformal meshes, where the single-surface RWG-discretization cannot be adopted.

Practically speaking, this choice makes sense because the modular analysis of composite objects, of great interest nowadays, is often tackled through the interconnection of domains that are meshed differently. Whereas for the composite objects the computed results are compared with the two-surface RWG-discretization of the EFIE–PMCHWT formulation, the accuracy in the monopolar-RWG analysis of the single dielectric objects with nonconformal meshes is checked against the standard RWG-implementation and conformal meshing except for the sphere, for which the analytical solution is available (Fig. 14).

We compute the volumetric integrals over wedges in our numerical tests through the decomposition of each wedge into three tetrahedral elements and the application of cubature rules of 11 points [42]. The surface and line integrals are computed with 9-point quadrature rules. The quasi-singular contributions of the kernel are computed analytically for the inner integrals of all the interactions. Whenever possible, for the sake of enhanced accuracy, the volumetric and surface field integrals are swapped with the line source integrals so that the well-known singularity subtraction techniques for triangles or tetrahedral elements [43] can be applied. In all the examples, the scattered fields are computed under an impinging $+z$ propagating $x$-polarized plane wave, and the free space wavelength $\lambda_0$ is set to 1 m.

### 4.1. Conformal meshes

We test the accuracy of our monopolar-RWG PMCHWT-implementations on several small sharp-edged targets with moderate or high relative permittivity; namely, a regular tetrahedron and a square pyramid, both with sides 0.1 m long. We choose such testing examples because the singular field behavior is observed at sharp edges and corners and, since the objects are electrically small, these singularities play an important role in the scattered fields.

We define the root-mean-square near-field relative error $e_{near}$ as [32]

$$e_{near} = \frac{[\sum_{j=1}^{K} |\tilde{\boldsymbol{E}}_s(\boldsymbol{r}_j) - \boldsymbol{E}_s^{REF}(\boldsymbol{r}_j)|^2 + \eta_0^2 \sum_{j=1}^{K} |\tilde{\boldsymbol{H}}_s(\boldsymbol{r}_j) - \boldsymbol{H}_s^{REF}(\boldsymbol{r}_j)|^2]^{1/2}}{[\sum_{j=1}^{K} |\boldsymbol{E}_s^{REF}(\boldsymbol{r}_j)|^2 + \eta_0^2 \sum_{j=1}^{K} |\boldsymbol{H}_s^{REF}(\boldsymbol{r}_j)|^2]^{1/2}} \tag{22}$$

where $\tilde{\boldsymbol{E}}_s(\boldsymbol{r}_j)$ and $\tilde{\boldsymbol{H}}_s(\boldsymbol{r}_j)$ denote the approximated scattered electric and magnetic fields computed with our PMCHWT implementations on a set of $K$ points $\{\boldsymbol{r}_1, \ldots, \boldsymbol{r}_K\}$ distributed around the target under analysis at very close distance (one tenth of the average mesh parameter adopted in the discretization). Similarly, we compute the root-mean-square relative bistatic RCS-error $e_{far}$ over a set of $M$ observation angles $\{\theta_1, \ldots, \theta_M\}$ in $E$ and $H$ plane

$$e_{far} = \frac{[\sum_{j=1}^{M} |RCS_E(\theta_j) - RCS_E^{REF}(\theta_j)|^2 + \sum_{j=2}^{M-1} |RCS_H(\theta_j) - RCS_H^{REF}(\theta_j)|^2]^{1/2}}{[\sum_{j=1}^{M} |RCS_E^{REF}(\theta_j)|^2 + \sum_{j=2}^{M-1} |RCS_H^{REF}(\theta_j)|^2]^{1/2}} \tag{23}$$

where $\theta_1 = 0$ and $\theta_M = \pi - \pi/M$ [32]. All the errors are computed with respect to reference results (REF) obtained with the conventional RWG-implementation of the PMCHWT formulation and very fine unstructured mesh (around 16300 triangles per target) with $h$-refinement near sharp edges and corners. The source integrals in the evaluation of near fields are computed with singularity subtraction technique and 9-point quadrature rules, while the integrals involved in the far-field computations are computed with a three-point rule. In our numerical tests we adopt $K = 400$ and $M = 60$ and all the testing elements in the monopolar-RWG implementations are defined conformal to the boundary to ensure maximum accuracy.

A) Accuracy versus $H$

In Figs. 6–9 we show the normalized errors of our monopolar-RWG PMCHWT-implementations, for the square pyramid (Figs. 6 and 8) and the regular tetrahedron (Figs. 7 and 9), and two moderately high dielectric contrasts ($\varepsilon_r = 40$ and $\varepsilon_r = 80$ for the square pyramid; $\varepsilon_r = 20$ and $\varepsilon_r = 50$ for the regular tetrahedron). We define the normalized RCS-error in Figs. 6 and 7 as [32]

$$\bar{e}_{far}^{tn} = e_{far}^{tn}/e_{far}^{R}, \quad \bar{e}_{far}^{vol} = e_{far}^{vol}/e_{far}^{R} \tag{24}$$

and, analogously, the normalized near-field error in Figs. 8 and 9 as [32]

$$\bar{e}_{near}^{tn} = e_{near}^{tn}/e_{near}^{R}, \quad \bar{e}_{near}^{vol} = e_{near}^{vol}/e_{near}^{R} \tag{25}$$

where the far-field errors $e_{far}^{tn}$, $e_{far}^{vol}$ and the near-field errors $e_{near}^{tn}$, $e_{near}^{vol}$ correspond to the definitions in (23) and (22), respectively, for the tangential-normal or volumetric PMCHWT implementations. Analogously, $e_{far}^{R}$ and $e_{near}^{R}$ denote the far-field and near-field errors computed with the RWG-discretization of the PMCHWT formulation and similar number of unknowns as the monopolar-RWG implementations. Hence, our implementations, which double the number of unknowns with respect to the conforming implementations, make use of a coarser mesh. Also, note how the normalized errors in Figs. 6–9 are plotted with respect to the height of the testing domains $H$, which in turn is set as a fraction of the mesh parameter $h$. In view of the definition of the normalized errors in (24) and (25), there is improved near- or far-field performance of the monopolar-RWG implementations with respect to the RWG-scheme as long as the corresponding normalized error, which is defined as the ratio between their respective relative errors, is smaller than one. Indeed, in case of observed improved

monopolar-RWG performance the relative error obtained with the monopolar-RWG implementation is smaller than the relative error computed with the RWG-scheme. Accordingly, the solid uniform line in Figs. 6–9 represents the upper bound of improved performance. Note that the results displayed in Figs. 6–9 assume a constant mesh parameter $h$ for each particular object and implementation, whereby the only varying parameter along the abscissa axis is $H$.

In view of Figs. 6 and 7, our monopolar-RWG implementations outperform the conventional RWG implementation in the far-field computation over the following $H$ ranges: between $H = h/1000$ and $H = h$ (tangential-normal), between $H =$

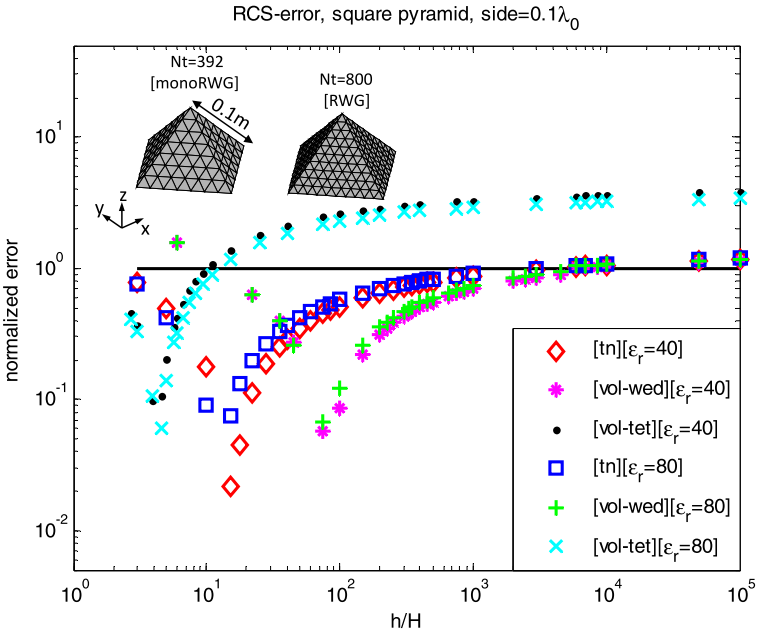


**Fig. 6.** Normalized RCS-error of our monopolar-RWG PMCHWT implementations, with respect to PMCHWT[R] and similar number of unknowns (around 2400) versus the height $H$ of the testing elements for a square pyramid with side 0.1 m ($\lambda_0 = 1$ m) and two relative permittivites (40 and 80). The reference results are obtained with PMCHWT[R] and a very fine mesh (around 16300 triangles).

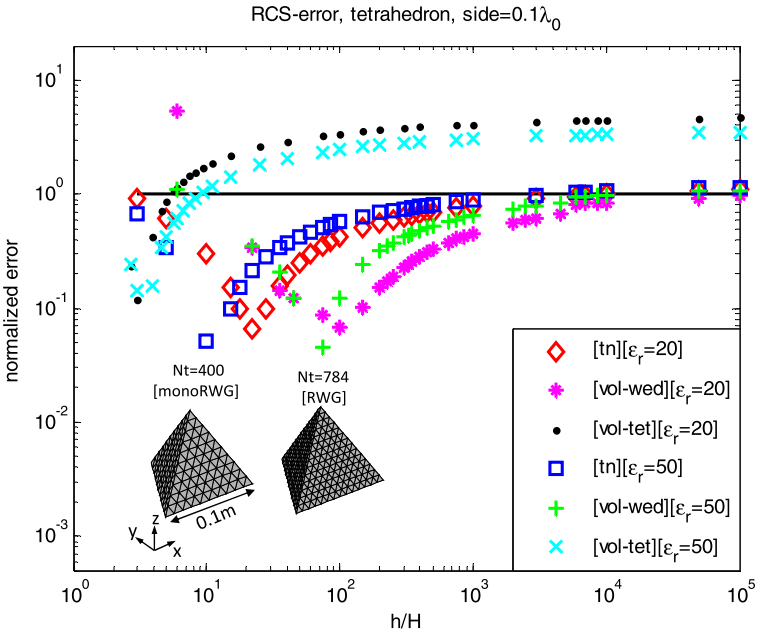


**Fig. 7.** Normalized RCS-error of our monopolar-RWG PMCHWT implementations, with respect to PMCHWT[R] and similar number of unknowns (around 2400) versus the height $H$ of the testing elements for a regular tetrahedron with side 0.1 m ($\lambda_0 = 1$ m) and two relative permittivites (20 and 50). The reference results are obtained with PMCHWT[R] and a very fine mesh (around 16300 triangles).

$h$/1e5 and $H = h/20$ (wedge-volumetric) or between $H = h/10$ and $H = h$ (tetrahedral-volumetric). Our best performing monopolar-RWG implementations (in terms of $H$) provide far-field normalized errors around 50 times smaller than the normalized errors observed for PMCHWT[R] and similar number of unknowns. Similarly, in light of Figs. 8 and 9, improved performance in the computation of the near fields is observed for the $H$ ranges between $h$ and $h$/1e4 in all cases and the best normalized errors of our monopolar-RWG implementations, in terms of $H$, are around eight times smaller than the normalized errors obtained with PMCHWT[R] and similar number of unknowns.

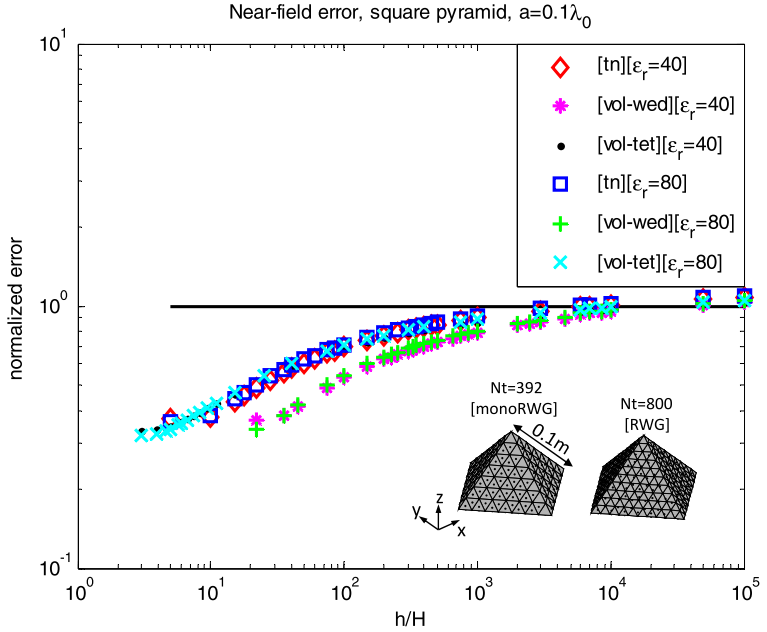


**Fig. 8.** Normalized near-field error of our monopolar-RWG PMCHWT implementations, with respect to PMCHWT[R] and similar number of unknowns (around 2400) versus the height $H$ of the testing elements for a square pyramid with side 0.1 m ($\lambda_0 = 1$ m) and two relative permittivites (40 and 80). The reference results are obtained with PMCHWT[R] and a very fine mesh (around 16300 triangles).

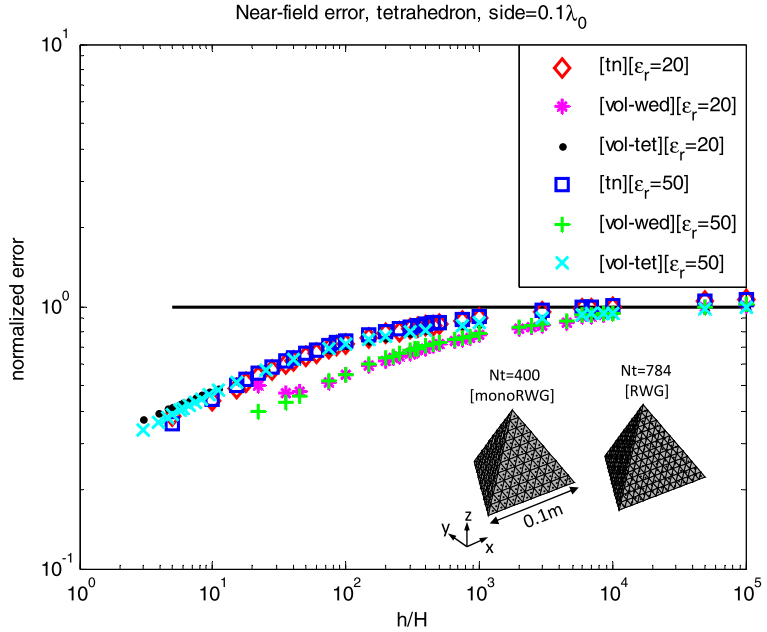


**Fig. 9.** Normalized near-field error of our monopolar-RWG PMCHWT implementations, with respect to PMCHWT[R] and similar number of unknowns (around 2400) versus the height $H$ of the testing elements for regular tetrahedron with side 0.1 m ($\lambda_0 = 1$ m) and two relative permittivites (20 and 50). The reference results are obtained with PMCHWT[R] and a very fine mesh (around 16300 triangles).

B) Accuracy versus $N$

We show the relative far-field and near-field errors, with respect to the number of unknowns $N$, for two sharp-edged targets with moderate dielectric contrasts and side $0.1\lambda_0$; namely, a regular tetrahedron with $\varepsilon_r = 50$ (Fig. 10) and a square pyramid with $\varepsilon_r = 40$ (Fig. 11). The height of the testing domains $H$ is chosen from the range of best performing heights displayed in Figs. 6–9. For all these examples the far-field and near-field errors observed for our monopolar-RWG implementations are smaller than the errors exhibited by the RWG-implementation. In Fig. 10 we observe a decrease in the RCS-error between $O(h)$ and $O(h^{1.5})$ with the tangential-normal and wedge testings and around $O(h^{0.6})$ with the tetrahedral testing. The RWG-implementation of the PMCHWT formulation exhibits an error reduction around $O(h^{0.6})$. In light of Fig. 11, all the implementations exhibit a reduction in the near-field errors around $O(h^{0.4})$.

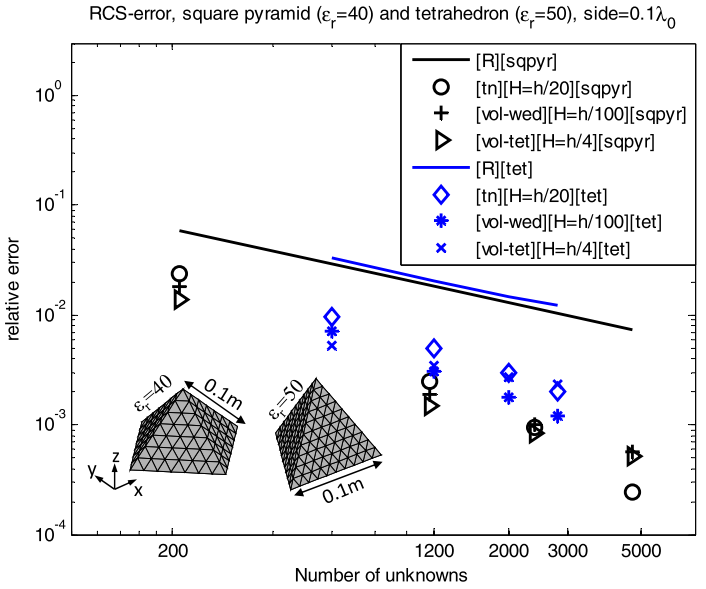


**Fig. 10.** RCS relative error of several monopolar-RWG PMCHWT implementations versus the number of unknowns for a regular tetrahedron with side 0.1 m and square pyramid with side 0.1 m ($\lambda_0 = 1$ m), and relative permittivities 40 and 50, respectively, for several values of testing heights $H$. The reference results are computed with PMCHWT[R] and very fine meshing (around 16300 triangles).

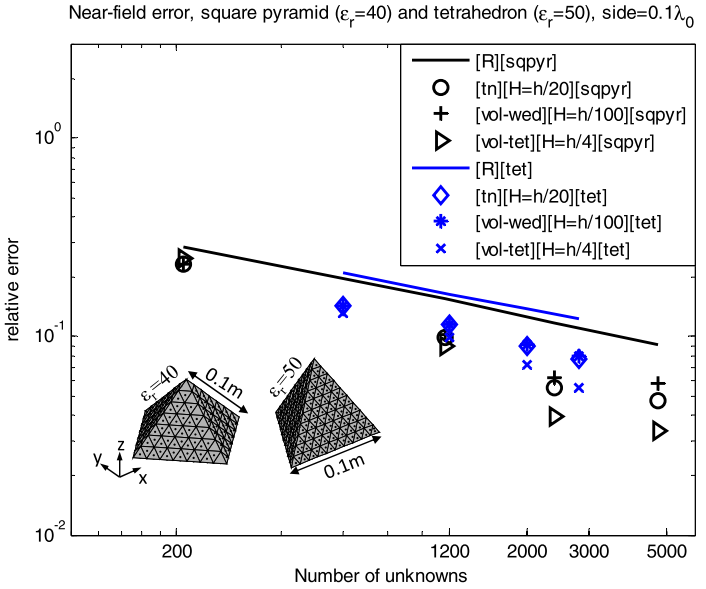


**Fig. 11.** Near-field relative error of several monopolar-RWG PMCHWT implementations versus the number of unknowns for a regular tetrahedron with side 0.1 m and square pyramid with side 0.1 m ($\lambda_0 = 1$ m), and relative permittivities 40 and 50, respectively, for several values of testing heights $H$. The reference results are computed with PMCHWT[R] and very fine meshing (around 16300 triangles).

### 4.2. Nonconformal meshes

We show RCS results of our monopolar-RWG EFIE–PMCHWT implementations for the scattering analysis of several objects, composite or single, discretized with nonconformal meshes. In Figs. 12 and 13, we show the computed bistatic RCS for two composite objects with dielectric or PEC regions. In Figs. 14 and 15, we show the bistatic RCS for two single dielectric targets, respectively, a dielectric sphere, with radius of 0.1 m and $\varepsilon_r = 15$, and a dielectric prism, with a square basis with side of 0.1 m, a height of 0.2 m and $\varepsilon_r = 3$. The nonconformal meshes employed in the composite objects of Figs. 12 and 13 arise from overlapping two nonmatching triangulations (see Fig. 5(c)). In contrast, the nonconformal meshes adopted in Figs. 14 and 15 arise from the interconnection of independently meshed open triangulations. Besides, for the dielectric sphere in Fig. 14, the resulting mesh is multi-scale and highly nonconformal, with spurious slits appearing where the coarse and fine touching triangulations meet. The testing domains in the monopolar-RWG EFIE–PMCHWT-implementations, for the sake of flexibility, are defined nonconformal to the boundary-surface. Indeed, this definition depends only on the corresponding surface triangle, with no insight into the facets around, which is appropriate in general for nonconformal meshes.

The standard single-surface RWG-implementation of the EFIE–PMCHWT formulation cannot handle the nonconformal meshes in Figs. 12 and 13 because the two triangulations sharing an interface do not match. Similarly, this conventional discretization cannot manipulate the nonconformal meshes in Figs. 14 and 15 because some adjacent triangles do not have single matching edges. For these reasons, the RCS results computed with our single-surface monopolar-RWG implementations in Figs. 12 and 13 are compared with the two-surface RWG-implementation ($\delta \to 0$) and similar number of unknowns. For the case of the dielectric sphere in Fig. 14, the RCS results computed with our monopolar-RWG schemes are compared with the Mie series solution [44] while for the case of dielectric prism, in Fig. 15, we compare our results with the solution obtained with the RWG-implementation of the PMCHWT formulation, a conformal mesh and similar number of unknowns. Note that in this paper we don't include the basic test example of a composite object discretized with a conformal mesh (see Fig. 5(a)). Indeed, the circumvention of junctions in the nonconforming analysis without sacrificing accuracy is already implicit in the observed results for the analysis of composite objects discretized with nonconformal meshes in Figs. 12 and 13, which are actually more challenging. As for the $H$-choice in the nonconforming analysis of the nonconformal meshes in Figs. 12, 13 and 15, we resort to Figs. 6 and 7, where the monopolar-RWG PMCHWT-implementations with wedge-volumetric or tangential-normal testing produce very similar accuracy as the RWG-discretization for very small values of $H$. Therefore, in Figs. 12, 13 and 15, we adopt $H = h/1e4$ for such monopolar-RWG implementations. Additionally, in light of Figs. 6 and 7, the tetrahedral scheme of testing deteriorates the accuracy for very small values of $H$, whereby our $H$-choice in Figs. 12, 13 and 15 lies within the successful range of $H$-values observed in Figs. 6 and 7. Furthermore, our tests suggest that the nonconforming analysis of the nonconformal mesh of the sphere in Fig. 14 represents a more demanding case because of the emergence of slits between adjacent nonconformal facets. Our experience for such cases shows that the adoption of bigger values of $H$ than the ones adopted for the nonconformal meshes with no slits in Figs. 12, 13 and 15 represents a better suited choice. In view of Figs. 12–15, very good agreement is observed in all the tested cases.

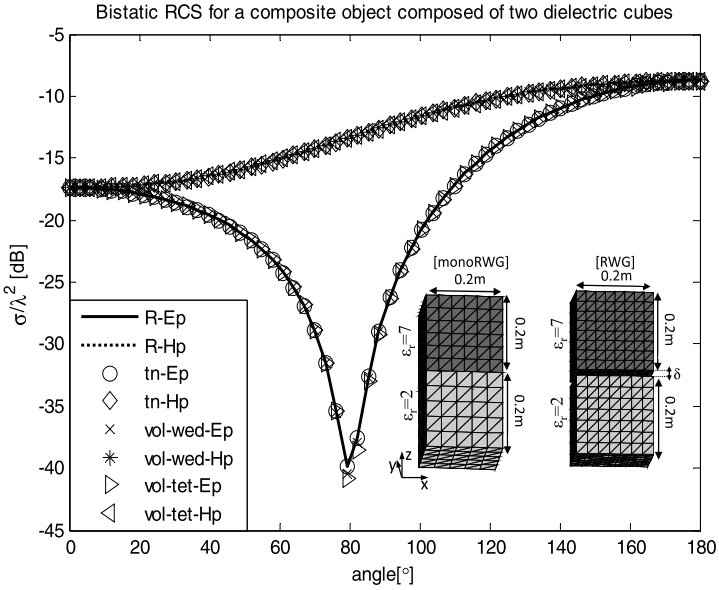


**Fig. 12.** Bistatic RCS of a composite object comprised of two dielectric cubes ($\varepsilon_r = 2$ and $\varepsilon_r = 7$) with sides of 0.2 m under an impinging $x$-polarized $+z$ propagating plane wave and $\lambda_0 = 1$ m. The number of unknowns is 4026 for our single-surface monopolar-RWG PMCHWT-implementations and 4068 for the double-surface RWG PMCHWT-implementation ($\delta \to 0$), which is adopted as reference. The implementations with tangential-normal and wedge volumetric testing use $H = h/1e4$ while the implementation with tetrahedral testing uses $H = h/5$.

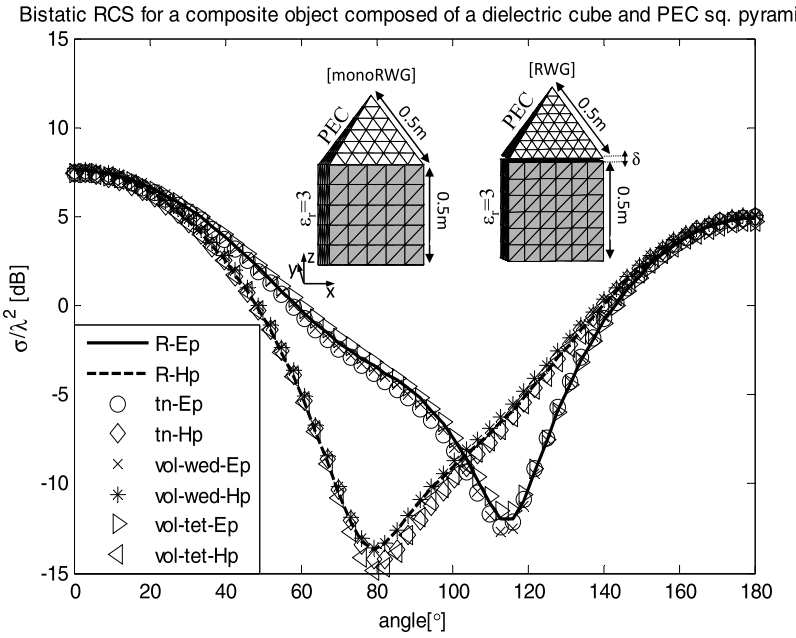


**Fig. 13.** Bistatic RCS of a composite object comprised of a dielectric cube ($\varepsilon_r = 3$, side = 0.5 m) and a PEC square pyramid (side = 0.5 m) under an impinging $x$-polarized $+z$ propagating plane wave and $\lambda_0 = 1$ m. The number of unknowns is 2946 for our single-surface monopolar-RWG PMCHWT-implementations and 2832 for the double-surface RWG PMCHWT-implementation ($\delta \to 0$), which is adopted as reference. The PMCHWT-implementations with tangential-normal and wedge testing use $H = h/1e4$ while the PMCHWT implementation with tetrahedral testing uses $H = h/5$.

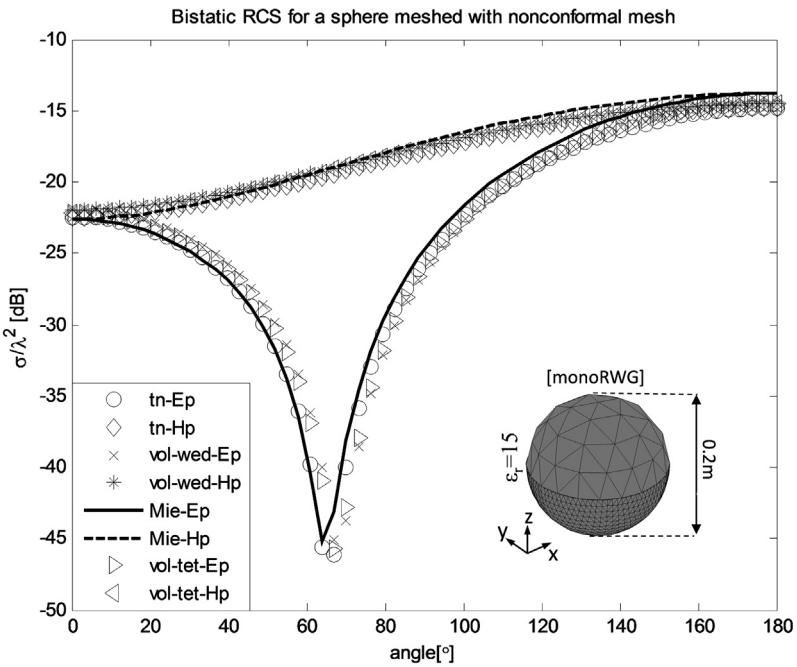


**Fig. 14.** Bistatic RCS of a dielectric sphere ($\varepsilon_r = 15$, $r = 0.1$ m) under an impinging $x$-polarized $+z$ propagating plane wave and $\lambda_0 = 1$ m. The number of unknowns is 4290 for our single-surface monopolar-RWG PMCHWT-implementations. The Mie series solution is adopted as reference. Tangential-normal and volumetric-wedge implementations use $H = h/10$ while volumetric-tetrahedral implementation uses $H = h/3$.

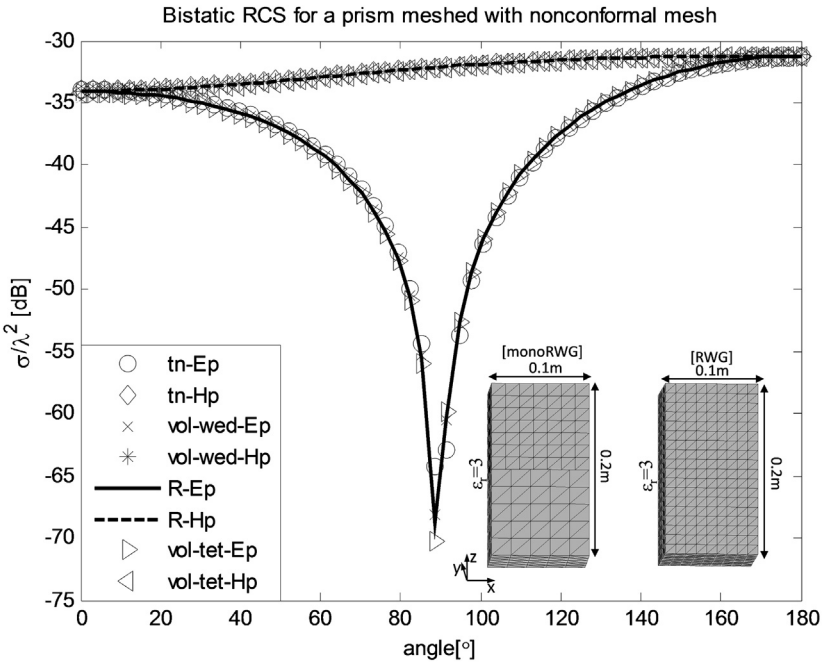


**Fig. 15.** Bistatic RCS of a dielectric prism ($\varepsilon_r = 3$) under an impinging $x$-polarized $+z$ propagating plane wave and $\lambda_0 = 1$ m. The prism basis is square with the side equal to 0.1 m. The height of the prism is 0.2 m. The number of unknowns is 2220 for our single-surface monopolar-RWG PMCHWT-implementations and 2430 for the RWG implementation, which is adopted as reference. The PMCHWT-implementations with tangential-normal and wedge testing use $H = h/1e4$ while the PMCHWT-implementation with tetrahedral testing uses $H = h/5$.

## 5. Conclusion

In this paper we introduce a nonconforming discretization of the EFIE–PMCHWT formulation applied to the single-surface scattering analysis of composite piecewise homogeneous objects with junctions. Just like the nonconforming discretization of the EFIE introduced in [27–29], we expand the electric and magnetic currents over the boundary interfaces of the target with the facet-based monopolar-RWG set and test the fields off the boundary, in the null-field region, with several non-Galerkin approaches; namely, tangential-normal, over pairs of triangles, or volumetric, over wedges or tetrahedral elements. Although the computation of the impedance matrix entries becomes somewhat more complicated when compared with the conventional conforming implementations, these facet-based schemes ignore by definition edges and junctions, which require a special treatment in the conventional single-surface RWG-approach [19–23]. Overall, hence, our facet-based schemes substantially reduce the programming burden and increase the flexibility of the method. Moreover, improved near-field and far-field accuracies are observed for our nonconforming PMCHWT implementations when compared with the conventional RWG-schemes for the tested electrically-small targets with sharp edges and corners and moderate or high relative permittivities (above 10). We attribute this improvement to the better singular-field modeling [32,41] in the vicinity of sharp edges with the adopted discontinuous basis functions together with the pertinent testing over volumetric or surface domains close to the boundary. The best performing heights of the testing elements off the boundary lie roughly between 50 and 1000 times smaller than the mesh parameter, for the tangential-normal and the wedge-volumetric testing schemes, and around the mesh parameter or down to 10 times smaller for the tetrahedral-volumetric implementation. In these cases, similar or better error decrease rates for a growing number of unknowns are observed with respect to the standard RWG-implementation. Consistently, the application of the proposed nonconforming schemes to the scattering analysis of targets with smooth surfaces and/or with low dielectric contrasts, where the singular field behavior does not appear [32,41], offers similar or slightly better accuracy than the conventional RWG formulation but doubling the number of unknowns. Finally, the analysis with our nonconforming schemes of single or composite penetrable objects meshed with nonconformal meshes becomes very satisfactory in terms of accuracy. These meshes, which the conventional edge-based schemes cannot handle, are used in the independent modular design of complex objects and arise from the juxtaposition of independently meshed domains, very often imported from CAD tools.

## Acknowledgements

This work was supported by FEDER and the Spanish Comisión Interministerial de Ciencia y Tecnología (CICYT) under projects TEC2013-47360-C3-1-P, TEC2016-78028-C3-1-P, TEC2017-84817-C2-2-R and the Unidad de Excelencia Maria de Maeztu MDM-2016-0600, which is financed by the Agencia Estatal de Investigación, Spain.

## References


[1] S.M. Rao, D.R. Wilton, A.W. Glisson, Electromagnetic scattering by surfaces of arbitrary shape, IEEE Trans. Antennas Propag. 30 (3) (May 1982) 409–418.
[2] T.K. Wu, L.L. Tsai, Scattering from arbitrarily-shaped lossy dielectric bodies of revolution, Radio Sci. 12 (Sep./Oct. 1977) 709–718.
[3] Y. Chang, R.F. Harrington, A surface formulation for characteristic modes of material bodies, IEEE Trans. Antennas Propag. 25 (6) (Nov. 1977) 789–795.
[4] A.J. Poggio, E.K. Miller, Integral equation solutions of three dimensional scattering problems, in: R. Mittra (Ed.), Computer Techniques for Electromagnetics, Pergamon, Oxford, UK, 1973, ch. 4.
[5] D.H. Schaubert, D.R. Wilton, A.W. Glisson, A tetrahedral modeling method for electromagnetic scattering by arbitrarily shaped inhomogeneous dielectric bodies, IEEE Trans. Antennas Propag. 32 (1) (Jan. 1984) 77–85.
[6] Jianming Jin, The Finite Element Method in Electromagnetics, Wiley–IEEE Press, April 2014.
[7] P.P. Silvester, R.L. Ferrari, Finite Elements for Electrical Engineers, 3rd ed., Cambridge University Press, Cambridge, 1996.
[8] J. Berenger, A perfectly matched layer for the absorption of electromagnetic waves, J. Comput. Phys. 114 (2) (1994) 185–200.
[9] R.F. Harrington, Field Computation by Moment Method, Macmillan, New York, NY, USA, 1968.
[10] P. Monk, Finite Element Methods for Maxwell's Equations, Clarendon, Oxford, UK, 2003.
[11] P. Ylä-Oijala, S.P. Kiminki, J. Markkanen, S. Järvenpää, Error controllable and well-conditioned MoM solutions in computational electromagnetics: ultimate surface integral-equation formulation, IEEE Antennas Propag. Mag. 55 (6) (Dec. 2013) 310–331.
[12] P. Ylä-Oijala, S.P. Kiminki, S. Järvenpää, Conforming testing of electromagnetic surface-integral equations for penetrable objects, IEEE Trans. Antennas Propag. 64 (6) (Jun. 2016) 2348–2357.
[13] K. Cools, F.P. Andriulli, D. De Zutter, E. Michielssen, Accurate and conforming mixed discretization of the MFIE, IEEE Antennas Wirel. Propag. Lett. 10 (Jun. 2011) 528–531.
[14] K. Umashankar, A. Taflove, S.M. Rao, Electromagnetic scattering by arbitrary shaped three-dimensional homogeneous lossy dielectric objects, IEEE Trans. Antennas Propag. 34 (6) (Jun. 1986) 758–766.
[15] R. Hiptmair, C. Schwab, Natural boundary element methods for the electric field integral equation on polyhedra, SIAM J. Numer. Anal. 40 (1) (2002) 66–86.
[16] A. Buffa, R. Hiptmair, T. von Petersdorff, C. Schwab, Boundary element methods for Maxwell transmission problems in Lipschitz domains, Numer. Math. 95 (3) (2003) 459–485.
[17] E. Arvas, Y. Qian, T.K. Sarkar, F. Aslan, TE scattering from a conducting cylinder of arbitrary cross section covered by multiple layers of lossy dielectrics, IEEE Proc. H-Microw. Antennas Propag. 136 (6) (Dec. 1989) 425–430.
[18] A.A. Kishk, W.A. Glisson, M.P. Goggans, Scattering from conductors coated with materials of arbitrary thickness, IEEE Trans. Antennas Propag. 40 (1) (Jan. 1992) 108–112.
[19] J.M. Putnam, L.N. Medgyesi-Mitschang, Combined field integral equation formulation for inhomogeneous two- and three-dimensional bodies: the junction problem, IEEE Trans. Antennas Propag. 39 (May 1991) 667–672.
[20] L.N. Medgyesi-Mitschang, J.M. Putnam, M.B. Gedera, Generalized method of moments for three-dimensional penetrable scatterers, J. Opt. Soc. Am. A 11 (4) (Apr. 1994) 1383–1398.
[21] B.M. Kolundzija, Electromagnetic modeling of composite metallic and dielectric structures, IEEE Trans. Microw. Theory Tech. 47 (7) (Jul. 1999) 1822–1825.
[22] M. Carr, E. Topsakal, J.L. Volakis, A procedure for modeling material junctions in 3-D surface integral equation approaches, IEEE Trans. Antennas Propag. 52 (5) (May 2004) 1374–1379.
[23] P. Ylä-Oijala, M. Taskinen, J. Sarvas, Surface integral equation method for general composite metallic and dielectric structures with junctions, Prog. Electromagn. Res. 52 (2005) 81–108.
[24] Y. Chu, W.C. Chew, J. Zhao, S. Chen, A surface integral equation formulation for low-frequency scattering from a composite object, IEEE Trans. Antennas Propag. 51 (10) (Oct. 2003) 2837–2844.
[25] Zhen Peng, Kheng-Hwee Lim, Jin-Fa Lee, Computations of electromagnetic wave scattering from penetrable composite targets using a surface integral equation method with multiple traces, IEEE Trans. Antennas Propag. 61 (January 2013) 256–270.
[26] E. Ubeda, J.M. Rius, Novel monopolar MoM-MFIE discretization for the scattering analysis of small objects, IEEE Trans. Antennas Propag. 54 (1) (Jan. 2006) 50–57.
[27] E. Ubeda, J.M. Rius, A. Heldring, Nonconforming discretization of the electric-field integral equation for closed perfectly conducting objects, IEEE Trans. Antennas Propag. 62 (8) (Aug. 2014) 4171–4186.
[28] E. Ubeda, J.M. Rius, A. Heldring, I. Sekulic, Volumetric testing parallel to the boundary surface for a nonconforming discretization of the electric-field integral equation, IEEE Trans. Antennas Propag. 63 (7) (Jul. 2015) 3286–3291.
[29] E. Ubeda, I. Sekulic, A. Heldring, J.M. Rius, Tangential-normal surface testing for the nonconforming discretization of the electric-field integral equation, Antennas Wirel. Propag. Lett. 15 (2016) 1581–1584.
[30] Z. Peng, K.H. Lim, J.F. Lee, A discontinuous Galerkin surface integral equation method for electromagnetic wave scattering from nonpenetrable targets, IEEE Trans. Antennas Propag. 61 (7) (Jul. 2013) 3617–3628.
[31] I. Sekulic, E. Ubeda, J.M. Rius, Tangential-normal line testing for a nonconforming discretization of the transversal-electric electric-field integral equation for 2D conductors, in: Proc. Int. Conf. Electromagn. Adv. Appl. (ICEAA), Turin, Italy, Sep. 2015, pp. 581–584.
[32] I. Sekulic, E. Ubeda, J.M. Rius, Versatile and accurate schemes of discretization in the scattering analysis of 2D composite objects with penetrable or perfectly conducting regions, IEEE Trans. Antennas Propag. 65 (5) (May 2017) 2494–2506.
[33] V.N. Nair, B. Shanker, Generalized method of moments: a framework for analyzing scattering from homogeneous dielectric bodies, J. Opt. Soc. Am. A 28 (3) (Mar. 2011) 328–340.
[34] Bei-Bei Kong, Xin-Qing Sheng, A discontinuous Galerkin surface integral equation method for scattering from multi-scale homogeneous objects, IEEE Trans. Antennas Propag. (2018).
[35] M.A.E. Bautista, F. Vipiana, M.A. Francavilla, J.A.T. Vasquez, G. Vecchi, A nonconformal domain decomposition scheme for the analysis of multiscale structures, IEEE Trans. Antennas Propag. 63 (8) (Aug. 2015) 3548–3560.
[36] Z. Peng, R. Hiptmair, Y. Shao, B. MacKie-Mason, Domain decomposition preconditioning for surface integral equations in solving challenging electromagnetic scattering problems, IEEE Trans. Antennas Propag. 64 (1) (Jan. 2016) 210–223.
[37] I. Sekulic, E. Ubeda, J.M. Rius, Nonconforming discretization of the PMCHWT integral equation applied to arbitrarily shaped dielectric objects, in: European Conference on Antennas and Propagation (EuCAP), Paris, Mar. 2017.
[38] E. Ubeda, J.M. Tamayo, J.M. Rius, Taylor-orthogonal basis functions for the discretizations in method of moments of second kind integral equations in the scattering analysis of perfectly conducting or dielectric objects, Prog. Electromagn. Res. 119 (2011) 85–105.
[39] Mei Song Tong, Weng Cho Chew, A novel approach for evaluating hypersingular and strongly singular surface integrals in electromagnetics, IEEE Trans. Antennas Propag. 58 (November 2010) 3593–3601.
[40] Gaobiao Xiao, Yibei Hou, Intuitive formulation of discontinuous Galerkin surface integral equations for electromagnetic scattering problems, IEEE Trans. Antennas Propag. 65 (January 2017) 287–294.

[41] J. Van Bladel, Singular Electromagnetic Fields and Sources, Clarendon, Oxford, UK, 1991.
[42] M. Gellert, R. Harbord, Moderate degree cubature formulas for 3-D tetrahedral finite element approximations, Commun. Appl. Numer. Methods 7 (1991) 487–495.
[43] D.R. Wilton, S.M. Rao, A.W. Glisson, D.H. Schaubert, O.M. Al-Bundak, C.M. Butler, Potential integrals for uniform and linear source distributions on polygonal and polyhedral domains, IEEE Trans. Antennas Propag. AP-32 (3) (Mar. 1984) 276–281.
[44] Gustav Mie, Beitrage zur Optik trüber Medien, speziell kolloidaler Metallösungen, Ann. Phys. 330 (3) (1908) 377–445.